Modelling approaches to the dewetting of evaporating thin films of nanoparticle suspensions

Modelling approaches to the dewetting of evaporating thin films of nanoparticle suspensions

U Thiele[1,3], I Vancea[1], A J Archer[1], M J Robbins[1], L Frastia[1],
A Stannard[2], E Pauliac-Vaujour[2], C P Martin[2], M O Blunt[2] and
P J Moriarty[2]

[1] Department of Mathematical Sciences, Loughborough University, Leicestershire LE11 3TU,
UK
[2] The School of Physics and Astronomy, The University of Nottingham, Nottingham NG7
2RD, UK

E-mail: u.thiele@lboro.ac.uk

Abstract

We review recent experiments on dewetting thin films of evaporating colloidal nanoparticle
suspensions (nanofluids) and discuss several theoretical approaches to describe the ongoing
processes including coupled transport and phase changes. These approaches range from
microscopic discrete stochastic theories to mesoscopic continuous deterministic descriptions. In
particular, we describe (i) a microscopic kinetic Monte Carlo model, (ii) a dynamical density
functional theory and (iii) a hydrodynamic thin film model.

Models (i) and (ii) are employed to discuss the formation of polygonal networks, spinodal
and branched structures resulting from the dewetting of an ultrathin 'postcursor film' that
remains behind a mesoscopic dewetting front. We highlight, in particular, the presence of a
transverse instability in the evaporative dewetting front, which results in highly branched
fingering structures. The subtle interplay of decomposition in the film and contact line motion is
discussed.

Finally, we discuss a simple thin film model (iii) of the hydrodynamics on the mesoscale.
We employ coupled evolution equations for the film thickness profile and mean particle
concentration. The model is used to discuss the self-pinning and depinning of a contact line
related to the 'coffee-stain' effect.

In the course of the review we discuss the advantages and limitations of the different
theories, as well as possible future developments and extensions.

(Some figures in this article are in colour only in the electronic version)

1. Introduction

The patterns formed in dewetting processes have attracted
strong interest since Reiter analysed the process quantitatively
in the early 1990s. In these experiments, that proved to be a
paradigm in our understanding of dewetting, a uniform thin
film of polystyrene (tens of nanometres thick) deposited on a
flat silicon oxide substrate is brought above the glass transition

temperature. The film ruptures in several places, forming
holes, which subsequently grow, competing for space. As a
result, a random polygonal network of liquid rims emerges.
The rims may further decay into lines of small drops due to
a Rayleigh-type instability [1–3]. The related problems of
retracting contact lines on partially wetting substrates and the
opening of single holes in rather thick films have also been
studied [4, 5].

Subsequent work has mainly focused on many different
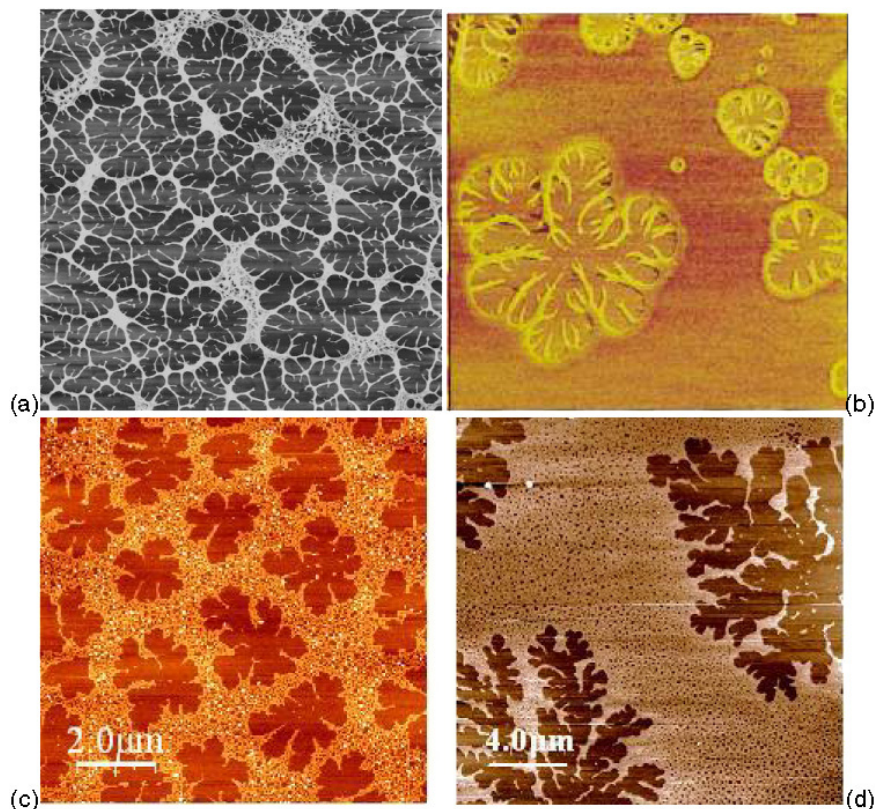aspects of the dewetting process for simple non-volatile

---

[3] http://www.uwethiele.de

1

Figure 1. Images of strongly ramified dewetting structures obtained using atomic force microscopy in the case of (a) an aqueous collagen solution on graphite (courtesy of Thiele, Mertig and Pompe; see also [42]; image size 5 μm × 5 μm); (b) poly(acrylic acid) in water spin-coated onto a polystyrene substrate (reprinted with permission from [23]; copyright 2002 John Wiley and Sons, Inc.; image size 2.5 μm × 2.5 μm); and in both (c) and (d), a solution of gold nanoparticles in toluene, spin-coated onto native oxide terminated silicon substrates (scale bars given in panels). In all the images, the lighter areas correspond to the deposited solute and the dark areas to the empty substrate.

liquids and polymers (for reviews see [6–8]). All stages of the dewetting of a film are studied: the initial film rupture via nucleation or a surface instability (called spinodal dewetting) [1, 9–13], the growth process of individual holes [14–16], the evolution of the resulting hole pattern [3, 13], and the stability of the individual dewetting fronts [17–19]. We note, in passing, that descriptions of dewetting patterns may also be found in historic papers, particularly for the dewetting of a liquid film on a liquid substrate. Tomlinson [20, footnote 18 on p 40] considered turpentine on water and Marangoni [21, p 352f] oil on water.

More recently, interest has turned to the dewetting processes of solutions and suspensions. However, these systems have not yet been investigated in any great depth. Such systems are complicated because their behaviour is determined by the interplay between the various solute (or colloid) and solvent transport processes. Furthermore, the solvents that are used often evaporate, i.e., one has to distinguish between 'normal' convective dewetting and evaporative dewetting. A number of experiments have been performed employing solutions of polymers [22–25], macromolecules like collagen and DNA [26–31] and nanoparticles [32–40]. The latter are sometimes referred to as 'nanofluids'. The initial focus of much of the research in the field has been on investigating the structures that are formed, which are similar to the ones

observed in the 'classical' dewetting of non-volatile liquids. Labyrinthine structures and polygonal networks result from spinodal dewetting and heterogeneous nucleation and growth, respectively. They are 'decorated' with the solute and therefore conserve the transient dewetting pattern as a dried-in structure when all the solvent has evaporated [28, 34]. The picture is, however, not complete. The solute may also shift the spinodal and binodal lines as compared to the locations of these lines in the phase diagram for the pure solvent [41]. As a consequence, the solute concentration influences the hole nucleation rate. More importantly, the solute particles may also destabilize the dewetting fronts. As a result, one may find strongly ramified structures in all three systems [42, 23, 40, 25]. A selection of images exhibiting some of the possible structures is displayed in figure 1.

For volatile solvents, the contact lines retract even for wetting fluids. It has been found that such evaporatively receding contact lines may deposit very regular line or ring patterns parallel to the moving contact line [43, 24]. The deposition of a single ring of colloids from a evaporating drop of colloidal suspension is well known as the 'coffee-stain effect' [44]. Detailed investigations reveal the emergence of rich structures including multiple irregular rings, networks, regular droplet patterns, sawtooth patterns, Sierpinski carpets, and—in the case of DNA—liquid

crystalline structures [45, 22, 46–49, 30]. The deposition of regularly spaced straight lines orthogonal to the moving contact line has also been reported [50]. Droplet patterns may also be created employing solvent-induced dewetting of glassy polymer layers below the glass transition temperature [51–53].

Note that the dewetting of pure volatile liquids has also been studied experimentally [54] and theoretically [55–58]. In this case, different contact line instabilities have been observed for evaporating liquid drops [59, 60].

In the present article we review and preview the experiments and in particular the various modelling approaches for dewetting suspensions of (nano)particles in volatile partially wetting solvents.　　After reviewing the basic experimental results in section 2, we discuss in section 3 several theoretical approaches. In particular, we present a kinetic Monte Carlo model in section 3.1, a dynamical density functional theory in section 3.2, and a thin film evolution equation in section 3.3. Finally, we conclude in section 4 by discussing advantages and shortcomings of the individual approaches and future challenges to all of them.

2. Experiments with nanoparticle solutions

We focus on experiments that use monodisperse colloidal suspensions of thiol-passivated gold nanoparticles in toluene [33, 34, 37, 38, 61, 40, 39]. The gold core of 2–3 nm diameter is coated by a layer of alkyl-thiol molecules. The length of the carbon backbone of the thiol used in the experiments ranges from six to 12 carbon atoms (C_6–C_{12}) [40]. By varying the chain length, one can control to a certain extent the particle–particle attraction. Normally, the solution is deposited on to a plain silicon substrate that is covered by the native oxide layer only [34]. However, one may locally change the wetting behaviour of the solvent by further oxidizing the substrate [38]. By adding excess thiol one can also vary the properties of the solvent [40].

Two different procedures are employed for the deposition of the solution on to the substrate: spin-coating or a meniscus technique [62, 61]. The choice is important as it strongly influences the evaporation rate and, as a result, the pattern formation process. When using spin-coating, one finds that, directly after deposition, evaporation competes with dewetting until all the solvent has evaporated. The resulting deposits of nanoparticles are imaged by atomic force microscopy (AFM). For spin-coated films, the evaporation rate is high and structuring is normally finished before the spin-coater is stopped. Conversely, the solvent evaporation rate is strongly decreased when employing the meniscus technique [61], i.e. by depositing a drop of solution on a Teflon ring that is wetted by the solvent. This allows for a better control of the process and enables the use of contrast-enhanced microscopy to observe the dewetting process *in situ* [40]. All pattern formation is confined to the region of the receding contact line of toluene, silicon and air. With both techniques one may find monomodal or bimodal polygonal networks [34], labyrinthine spinodal structures, or branched patterns (see figure 1). The meniscus technique allows for the study of branched structures in a more controlled manner. The work in [40] indicates that fingering

strongly depends on the interaction strength of the particles, i.e., on the chain length of the thiol molecules coating the gold cores. For short chains (C_5 and C_8) no formation of branched structures is observed. At similar concentrations, well developed branched structures are formed for longer chains (C_{10} and C_{12}). For even longer chains (C_{14}), however, one again finds less branching. It also depends on the amount of excess thiol in the solvent (for details see [40]).

When following the evolution of the branched patterns *in situ* (see the complementary video material of [40]), one clearly observes that different processes occur on different length scales. First, a macroscopic dewetting front recedes, leaving behind a seemingly dry substrate. The macroscopic front can be transversely unstable, resulting in large-scale (>100 μm) strongly anisotropic fingered structures. For fronts that move relatively quickly these macroscopic structures cover all the available substrate. However, when at a later stage the macroscopic front becomes slower, these fingers become scarce and 'macroscopic fingering' finally ceases. At this stage it is possible to appreciate that the seemingly dry region left behind by the front is not at all dry, but covered by an ultrathin 'postcursor' film that is itself unstable. The thickness of this film is similar to the size of the nanoparticles. At a certain distance from the macroscopic front, the ultrathin film starts to evolve a locally isotropic pattern of holes. The holes themselves grow in an unstable manner resulting in an array of isotropically branched structures as shown, e.g., in figure 1. This indicates that at least some of the patterns described in the literature may have arisen from processes in similar ultrathin 'postcursor' films.

The existence of the ultrathin 'postcursor' film is an experimental finding that can be drawn on when choosing a theoretical approach to account for the pattern formation (see below). Note, however, that at the moment there exists no explanation for its existence. A possible hypothesis is that the substrate strongly attracts the nanoparticles. As a result they form a dense suspension layer having a thickness roughly equal to the diameter of the nanoparticles. The observed mesoscopic dewetting front then actually correspond to an autophobic dewetting of a low concentration suspension from the higher concentration suspension on the surface of the substrate.

3. Modelling approaches

Models of dewetting thin films of pure liquids or polymers are often based on thin film hydrodynamics. Starting from the Stokes equations, together with continuity and boundary conditions at the substrate and free surface, one applies a long-wave approximation (assuming small surface slopes and contact angles) [63, 8] and obtains a nonlinear evolution equation for the film thickness profile $h(x, y, t)$. In the case of volatile liquids one finds [55–58, 64]

$$\partial_t h = \nabla \left[Q_c \nabla \frac{\delta F}{\delta h} \right] - Q_e \frac{\delta F}{\delta h}, \qquad (1)$$

with the mobility functions $Q_c(h) = h^3/3\eta \geqslant 0$ (assuming Poiseuille flow in the film and no slip at the substrate; η

is the dynamic viscosity) and $Q_e \geqslant 0$ for the convective and evaporative part of the dynamics, respectively. Q_e is a rate constant that can be obtained from gas kinetic theory or from experiment [57]. Note that equation (1) only applies if the pressure in the vapour above the film is close to the saturation pressure. For alternative expressions that are used to describe the non-conserved evaporative dynamics see, e.g., [65, 66, 56, 67, 68, 57, 69]. Finally, $\nabla = (\partial_x, \partial_y)$, and ∂_t, ∂_x and ∂_y denote partial derivatives w.r.t. time and the coordinates.

Focusing on the influence of capillarity and wettability only, the energy functional $F[h]$ is given by

$$F[h] = \int \mathrm{d}x \int \mathrm{d}y \left[\frac{\gamma}{2} (\nabla h)^2 + f(h) - \mu h \right] \quad (2)$$

where γ is the liquid–gas surface tension and $f(h)$ is a local free energy term that describes the wettability of the surface. Since μ corresponds to a chemical potential, the term μh may either bias the system towards the liquid or towards the gas state. The variation of F w.r.t. h gives the pressure. It contains the curvature (Laplace) pressure $-\gamma \Delta h$ and the disjoining pressure $\Pi(h) = -\partial_h f(h)$. Many different forms for the latter are in use (see, e.g., [4, 70–72, 63, 73, 8]).

For the present system a thin film description using equation (1) is not appropriate because the nanoparticles are not taken into account. However, under certain conditions one can augment equation (1) for the evolution of the film thickness by coupling it to an equation for the evolution of the mean particle concentration. The resulting model is able to describe the behaviour of an evaporating solution on the meso- and macroscale. Such an approach is briefly discussed below in section 3.3. We should expect such a model to describe the mesoscopic dewetting front discussed above. However, the theory is less suited to a description of the dewetting dynamics of the ultrathin postcursor film.

The dewetting of the ultrathin film of highly concentrated suspension may be described by a discrete stochastic model such as, for instance, a kinetic Monte Carlo (KMC) model based solely on evaporation/condensation dynamics of the solvent and diffusion of the solute [35, 39, 41]. The validity of this strong assumption regarding the relevant transport processes can be confirmed from an estimate based on equation (1). The pressure $p = \delta F / \delta h$ drives convection and evaporation. The convective mobility is proportional to h^3; i.e., it is large for thick films but decreases strongly with reduced film thickness. The evaporative mobility, however, is a constant, implying that evaporation will dominate below a certain (cross-over) thickness. For the parameter values of [57] and a small contact angle (≈ 0.01), the cross-over thickness is in the range of 1–5 nm. This estimate justifies the neglect of convective transport in a description of the postcursor film and may explain why one has such good agreement between the experimentally observed patterns and the patterns obtained from a purely two-dimensional (single layer) kinetic Monte Carlo model [35]. We introduce the KMC model below in section 3.1.

In several respects, however, the kinetic Monte Carlo model is rather simplistic, limiting its potential applications.

For instance, the thermodynamic chemical potential as well as any wetting interaction of the solvent with the substrate are collected in a single parameter—an effective chemical potential. This implies that any influence of a disjoining pressure is 'smeared out' over the whole system and that no distinction between the short- and the long-range parts of the disjoining pressure is possible. It is furthermore based on the assumption that evaporation/condensation is the dominant dynamic process, but does not allow one to probe this assumption. In section 3.2 we show how one may develop a dynamical density functional theory (DDFT) that describes the system at a similar level to the KMC. However, the DDFT may also be easily extended to include other effects such as fluid diffusion, that the KMC does not incorporate.

3.1. Kinetic Monte Carlo model

The kinetic Monte Carlo model for two-dimensional dewetting nanofluids [33] was first proposed in [35] and extended to include next-nearest neighbour interactions in [37]. The two key assumptions used are that (i) the relevant processes can be mapped on to a two-dimensional lattice gas model, thereby neglecting continuous changes in the thickness of the evaporating film, and (ii) all relevant dynamics results from diffusing nanoparticles and evaporating/condensing solvent.

The model builds on an Ising-type model for the liquid–gas phase transition. The surface is divided up into a regular array of lattice sites whose size is dictated by the nanoparticles. One then considers each lattice site to be occupied either by a nanoparticle, liquid or vapour. This effectively maps the system onto a two-dimensional two-component lattice gas having two fields n and l. The resulting three possible states of a cell are liquid ($l = 1, n = 0$), nanoparticle ($l = 0, n = 1$), and vapour ($l = 0, n = 0$, i.e. cell empty). The energy of an overall configuration is given by the Hamiltonian

$$E = -\frac{\varepsilon_{nn}}{2} \sum_{\langle ij \rangle} n_i n_j - \frac{\varepsilon_{nl}}{2} \sum_{\langle ij \rangle} n_i l_j - \frac{\varepsilon_{ll}}{2} \sum_{\langle ij \rangle} l_i l_j - \mu \sum_i l_i \quad (3)$$

where $\sum_{\langle ij \rangle}$ denotes a sum over nearest neighbour pairs and ε_{ll}, ε_{nn} and ε_{nl} are the liquid–liquid, particle–particle and liquid–particle interaction energies, respectively. Fixing the three interaction strength parameters ε_{ll}, ε_{nn}, ε_{nl} and the effective chemical potential μ determines the equilibrium state of the system. We choose ε_{ll} as unit of energy—i.e., we set $\varepsilon_{ll} = 1$.

The Hamiltonian determines the equilibrium state and the energy landscape of the system. However, as the system 'dries in' during the course of the solvent evaporation, the final nanoparticle configurations do not necessarily represent equilibrium structures. This implies that the system dynamics is of paramount importance. It is determined by the possible Monte Carlo moves, their relative frequencies, and the probabilities for their acceptance. Two types of moves are allowed: (i) evaporation/condensation of liquid and (ii) diffusion of nanoparticles within the liquid. A mobility M corresponds to the ratio of cycles of particle and solvent moves and reflects the physical ratio of timescales for evaporation and diffusion. A large mobility M indicates fast diffusion as compared to evaporation. A trial move is accepted with the
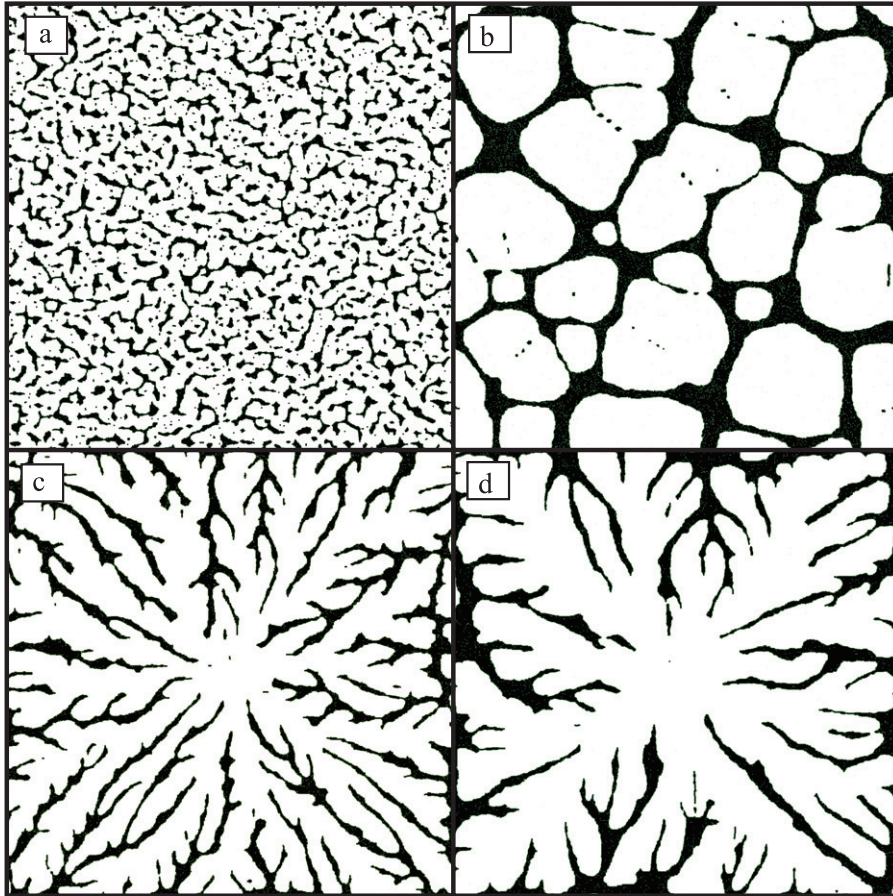
Figure 2. Typical KMC results for the final dried-in nanoparticle structures resulting from the evaporative dewetting processes of nanoparticle solutions (nanofluids) in the case of (a) a spinodal-like process at $\mu = -2.55$, (b) nucleation and growth of holes at $\mu = -2.3$, (c) unstable fronts at $\mu = -2.3$ and low mobility $M = 5$, and (d) unstable fronts at $\mu = -2.3$ and medium mobility $M = 10$. The starting configuration in (a) and (b) is a homogeneous liquid film with uniformly distributed particles whereas in (c) and (d) a hole at the centre is nucleated 'by hand'. The remaining parameters are ((a), (b)) $M = 50$, $\epsilon_{nl} = 2.0$, $\epsilon_{nn} = 1.5$, $\rho_n^{av} = 0.2$, $kT = 0.3$, MC steps = 500, domain size 1200×1200; ((c), (d)) $\varepsilon_{nn} = 2.0$, $\epsilon_{nl} = 1.5$, $\rho_n^{av} = 0.2$, $kT = 0.2$, MC steps = 3000, domain size 1200×1200. Lattice sites occupied by particles are coloured black, and the empty sites are coloured white.

probability $p_{acc} = \min[1, \exp(-\Delta E/kT)]$, where k is the Boltzmann constant, T the temperature and ΔE the change in energy resulting from the potential move. Note that particles are only allowed to move into wet areas of the substrate, i.e. onto cells with $l = 1$. This models zero diffusivity of the particles on a dry substrate. The replaced liquid fills the site left by the nanoparticle.

Without nanoparticles, the behaviour of the model is well known, as it reduces to the classical two-dimensional Ising model [74]. For $kT < kT_c \approx 0.567$ liquid and vapour coexist when $\mu = \mu_{coex} = -2$. For $\mu > -2$ ($\mu < -2$) eventually the liquid (vapour) dominates. A straight liquid–gas interface will recede (advance) for $\mu < -2$ ($\mu > -2$); i.e., one finds evaporative dewetting (wetting) fronts. If one starts, however, with a substrate covered homogeneously by the liquid, for $\mu < -2$ the film will dewet via a nucleation or spinodal-like process. If the nanoparticles are present, they form dried-in structures when all the liquid evaporates. The final structures do not normally change any further—at least on short timescales. However, if the liquid wets the particles (i.e. is attracted to the particles), over long times there might

be a coarsening of the structures, facilitated by the adsorbed liquid. The dried-in patterns depend on the particular pathway taken by the evaporative dewetting process. They range from labyrinthine to polygonal network structures or holes in a dense particle layer. Some typical patterns are displayed in figure 2, for cases when the average surface coverage of the nanoparticles $\rho_n^{av} = 0.2$. Panels (a) and (b) result from a spinodal-like and nucleation and growth process, respectively. At first sight they look very similar to the patterns seen for the pure solvent and one might argue that the particles solely act as passive tracers and preserve the transient volatile dewetting structures of the solvent. This was suggested in [26–28] for dewetting collagen solutions. However, panels (c) and (d) indicate that the particles may at times play a rather more significant role. When the diffusion of the particles is slow, the evaporative dewetting fronts become transversely unstable and may result in strongly ramified patterns. This instability is caused by the nanoparticles. The lower their mobility, the stronger the fingering effect; i.e., there are more fingers in (c) than in (d) because in the latter the mobility is larger.

The front instability is intriguing as it results in strongly branched structures. As the dewetting front moves, new branches are continuously created and existing branches merge at the moving contact line. However, the mean finger number in the streamwise direction of the resulting ramified pattern is roughly a constant. This behaviour is in contrast to the front instabilities found for dewetting polymers, which only result in fingers without side branches [75] or fields of droplets left behind [18].

A quantitative analysis shows that the mean number of fingers depends only very weakly on the average concentration of the nanoparticles ρ_n^{av}; only the mean finger width increases with increasing concentration. However, decreasing the mobility (i.e. decreasing the diffusivity of the particles) leads to a much denser finger pattern and also causes the front instability to appear at an earlier stage; i.e., when the front instability is in its initial linear regime, it has a higher growth rate and a smaller characteristic wavelength (cf. figures 2(c) and (d)). Decreasing the effective chemical potential (increasing its absolute value) has a similar but less strong effect. For details see [41]. These findings lead to the conclusion that the determining factor for the front instability is the ratio of the timescales of the different transport processes. In particular, the front becomes more unstable when the velocity of the dewetting front increases as compared to the mean diffusion velocity of the nanoparticles.

If the particle diffusivity is low, the front 'collects' the particles, resulting in a build-up of the particles at the front that itself is slowed down. This makes the front unstable and any fluctuation along the front will trigger a transverse instability that results in an evolving fingering pattern. This happens even when the particle–liquid and particle–particle attractive interactions do not favour clustering (i.e. demixing of the liquid and the nanoparticles). In this regime, the instability is a purely dynamic effect and energetics plays no role in determining the number of fingers. We call this the 'transport regime'.

To illustrate the influence of energetics (characterized by the interaction parameters ε_{ij}) on fingering, in figure 3 we display the dependence of the mean finger number on particle–liquid interaction strength ε_{nl}. For $\varepsilon_{nl} \geqslant 1.5$ the mean finger number $\langle f \rangle$ is nearly constant; this is the transport regime. However, on decreasing ε_{nl} below 1.5 we observe a marked increase in the value of $\langle f \rangle$, indicating that energy plays an important role in determining the number of fingers in this regime. In this parameter range, demixing of particles and liquid occurs at the moving front and increases its transverse instability. In this 'demixing regime', the wavelength of the fingering instability is determined by the dynamics *and* the energetics of the system. Decreasing ε_{nl} further (below 1.4 in figure 3) one first observes in regime (iii) a slight decrease in the average finger number. This is a geometric effect resulting from our one-dimensional finger counting routine. The fingers increasingly break up and the dried-in pattern looks progressively isotropic. In regime (iv), the measure $\langle f \rangle$ does not represent a finger number but instead indicates a decrease in the typical distance between particle clusters resulting from the demixing process that occurs already in the bulk liquid and is not related to the front instability at all. Note that one
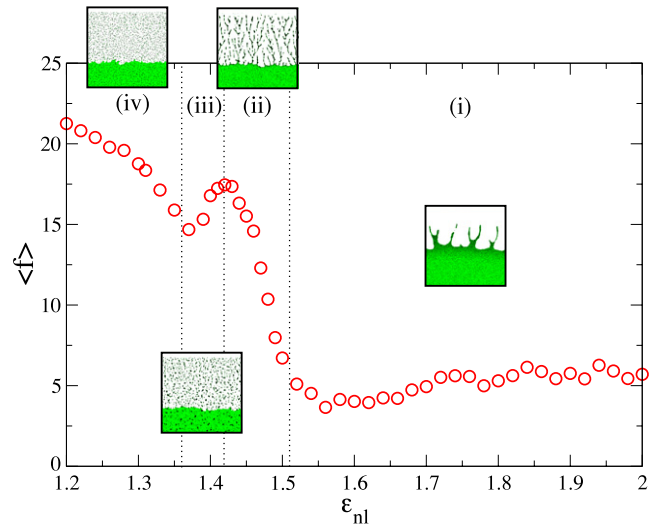

Figure 3. Dependence of the mean finger number left behind by the unstable dewetting front on the particle–liquid interaction strength ε_{nl}. The regions marked (i) to (iv) are discussed in the main text. The insets display typical snapshots obtained in the four different regions. Particles are black, liquid is grey (green online) and the empty substrate is white. The remaining parameters are $kT = 0.2$, $M = 20$, $\mu = -2.2$, $\rho_n^{av} = 0.1$, $\epsilon_{nn} = 2.0$, domain size 1200×1200. For the insets, from left to right, $\epsilon_{nl} = 1.2, 1.4, 1.45, 1.8$.

finds a similar sequence of regimes (i)–(iv) when increasing the particle–particle interaction strengths for fixed ε_{nl} (see [41]) for further details.

We note also that the fingering process may be viewed as self-optimizing the front motion—i.e., the front keeps its average velocity constant by expelling particles into the fingers. A similar effect exists for dewetting polymer films [18], where liquid is expelled from the growing moving rim, which collects the dewetted polymer. There, the surplus liquid is left on the surface as a droplet pattern.

The kinetic Monte Carlo model is a very useful tool that helps one to understand the pattern formation in drying nanoparticle suspensions. One has, however, to keep in mind the restrictions on the model (see above). The purely two-dimensional character of the KMC was extended to a 'pseudo-three-dimensional' one by making the effective chemical potential dependent on the mean liquid coverage [38]. As the latter is related to a mean film thickness, this corresponds to the introduction of a 'global' thickness dependent disjoining pressure into the evaporation term without an explicit consideration of a film thickness. The amended model can reproduce bimodal structures that are beyond the scope of the purely two-dimensional model [38, 39]. Fully three-dimensional models are also discussed in the literature [76, 77].

3.2. Dynamical density functional theory

The limitations of the kinetic Monte Carlo model introduced in section 3.1 are related to its character as a two-dimensional lattice gas with only three states: gas, liquid or particle. This implies that (i) no liquid can be transported to a site on the surface already filled with liquid, i.e., diffusion of the liquid cannot be incorporated in a sensible way, and (ii) one is not able

to distinguish between the influence of the short- and the long-range parts of the interactions with the substrate, as all such interactions are absorbed into the effective chemical potential.

However, using dynamical density functional theory (DDFT) [78–83] one can develop a model for the processes in the ultrathin postcursor film without these limitations, although here we limit ourselves to developing the theory at the level of the KMC and solely discuss how to extend it to incorporate the influence of the liquid diffusion over the surface. Such a DDFT model describes the coupled dynamics of the density fields of the liquid ρ_l and the nanoparticles ρ_n. The densities ρ_l and ρ_n are defined as the probabilities of finding a given lattice site on the surface to be occupied by a film of liquid or by a nanoparticle, respectively. Note that the probability densities correspond to number densities as we use the lattice spacing $\sigma = 1$ as our unit of length.

To develop the DDFT, one must first derive the underlying free energy functional $F[\rho_l, \rho_n]$, and second devise dynamical equations for both density fields that account for the conserved and the non-conserved aspects of their dynamics, i.e. transport and phase change processes, respectively.

For a system governed by the Hamiltonian (3), we may construct a mean-field (Bragg–Williams) approximation for the free energy of the system [84, 78] which contains an entropic contribution and contributions from the interactions between the different species (nanoparticles and liquid). The free energy is a semi-grand free energy, since the liquid is treated grand canonically (it is coupled to a reservoir with chemical potential μ), whereas the nanoparticles are treated in the canonical ensemble. The free energy functional is first defined on the original KMC lattice. However, after re-writing the interaction terms employing gradient operators [78] one finally obtains the free energy functional for a continuous system

$$F[\rho_l, \rho_n] = \int d\mathbf{r}\left[f(\rho_l, \rho_n) + \frac{\varepsilon_{ll}}{2}(\nabla\rho_l)^2 + \frac{\varepsilon_{nn}}{2}(\nabla\rho_n)^2 \right.$$
$$\left. + \varepsilon_{nl}(\nabla\rho_n)(\nabla\rho_l) - \mu\rho_l \right], \qquad (4)$$

where

$$f(\rho_l, \rho_n) = kT[\rho_l \ln\rho_l + (1-\rho_l)\ln(1-\rho_l)]$$
$$+ kT[\rho_n \ln\rho_n + (1-\rho_n)\ln(1-\rho_n)]$$
$$- 2\varepsilon_{ll}\rho_l^2 - 2\varepsilon_{nn}\rho_n^2 - 4\varepsilon_{nl}\rho_n\rho_l. \qquad (5)$$

Since the liquid may evaporate from the surface into the vapour above the surface, μ is the (true) chemical potential of this reservoir and determines the rate of evaporation (condensation) from (to) the surface. Note that normally a free energy of the form in equation (4) is obtained by making a gradient expansion of the free energy functional of a continuous system [84]. However, here we have made the mapping from the free energy of the lattice KMC system.

The chemical potential for the nanoparticles may be determined from the functional derivative $\mu_n = \delta F[\rho_n, \rho_l]/\delta\rho_n(\mathbf{r})$. In equilibrium it is constant throughout the system, but it may vary spatially in a non-equilibrium system, i.e., $\mu_n = \mu_n(\mathbf{r}, t)$. We assume that the dynamics of the nanoparticles is governed by the thermodynamic force

$\nabla\mu_n$—i.e. that the nanoparticle current is $\mathbf{j} = -M_n\rho_n\nabla\mu_n$, where $M_n(\rho_l)$ is a mobility coefficient that depends on the local density of the liquid. Combining this expression for the current with the continuity equation, we obtain the following evolution equation for the nanoparticle density profile:

$$\frac{\partial\rho_n}{\partial t} = \nabla\left[M_n\rho_n\nabla\frac{\delta F[\rho_n, \rho_l]}{\delta\rho_n} \right]. \qquad (6)$$

Note that this equation of motion may also be obtained by assuming that the nanoparticles have over-damped stochastic equations of motion [80–83]. Here, we assume that $M_n(\rho_l) = \alpha\Theta_s(\rho_l - 0.5)$, where $\Theta_s(x)$ is a continuous function that switches smoothly from zero value to unit value at $x = 0$ (i.e., it is essentially a smooth analogue of the Heaviside function). This ensures that the nanoparticles are immobile when the local liquid density is small (dry substrate) and have a mobility coefficient α when ρ_l is high (wet substrate).

For the evolution of the liquid density distribution we assume that the liquid is able to evaporate from the surface into the vapour (reservoir) above the surface (non-conserved dynamics) and may also diffuse over the substrate (conserved dynamics). The conserved part is treated along the lines developed above for the nanoparticles. For the non-conserved part we assume a standard form [85]; i.e., the change in time of ρ_l is proportional to $-(\mu_{surf}(\mathbf{r}, t) - \mu) = -\delta F[\rho_n, \rho_l]/\delta\rho_l(\mathbf{r})$, where $\mu_{surf}(\mathbf{r}, t)$ is the local chemical potential of the liquid at the point $\mathbf{r}$ on the surface at time t. This gives the evolution equation for the liquid density

$$\frac{\partial\rho_l}{\partial t} = \nabla\left[M_l^c\rho_l\nabla\frac{\delta F[\rho_n, \rho_l]}{\delta\rho_l} \right] - M_l^{nc}\frac{\delta F[\rho_n, \rho_l]}{\delta\rho_l}, \qquad (7)$$

where we assume that the coefficients M_l^c and M_l^{nc} are constants.

This theory allows us to study the time evolution of the evaporating film of nanoparticle suspension without some of the restrictions of the kinetic Monte Carlo model. Here, however, we illustrate its application in similar parameter regimes as used above for the KMC. We focus on two examples: (i) the spinodal dewetting of a initially flat film of nanoparticle suspension characterized by constant ρ_l and ρ_n (figure 4); (ii) the retraction of a dewetting front that is unstable with respect to a fingering instability (figure 5).

Figure 4 presents two pairs of snapshots from a purely evaporative dewetting process deep inside the parameter region of the phase diagram where spinodal dewetting occurs. For small times the film becomes unstable, showing a typical spinodal labyrinthine pattern with a typical wavelength. The nanoparticles concentrate where the remaining liquid is situated. However, they are 'slow' in their reaction: when ρ_l already takes values in the range 0.08–0.83, the nanoparticle concentration has only deviated by about 25% from its initial value. The film thins strongly, forming many small holes. The competition for space results in a fine-meshed polygonal network of nanoparticle deposits. The concentration of particles is much higher at the network nodes—an effect that cannot been seen within the KMC model. As the particles attract the liquid there remains some liquid on the substrate where the nanoparticles are.
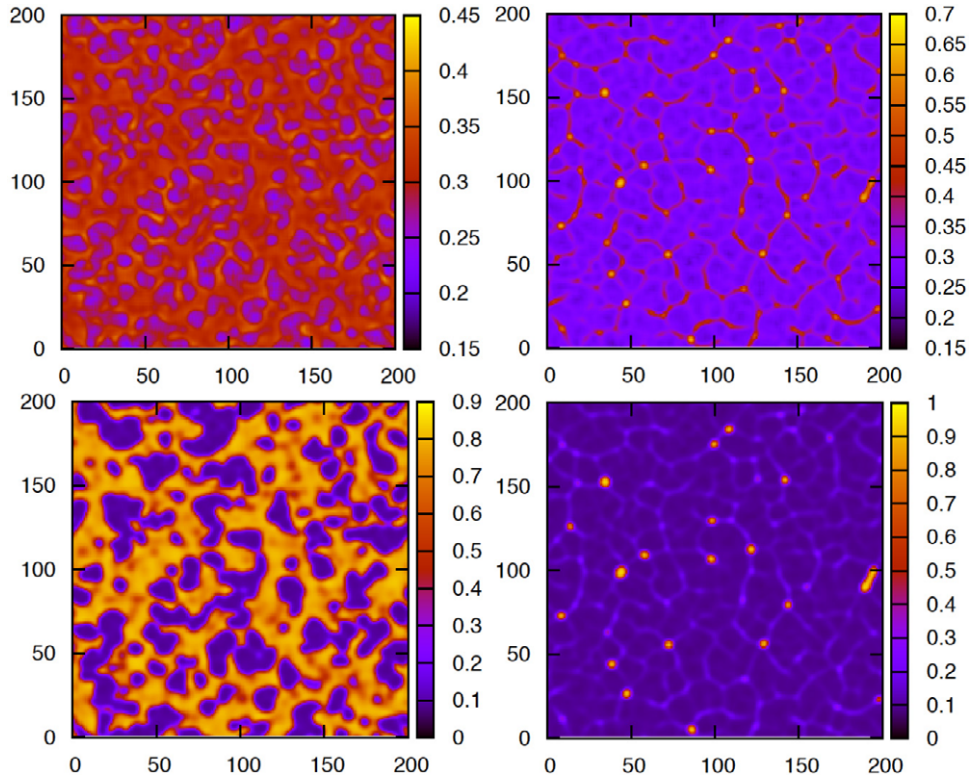
Figure 4. Density profiles for the situation where the substrate is covered by nanoparticles with average density $\rho_n^{av} = 0.3$. The top row is the nanoparticle density profiles and the bottom row is the corresponding liquid density profiles at the times $t/t_1 = 8$ (left) and 80 (right), where $t_1 = 1/kT M_1^{nc} \sigma^2$. The parameters are $kT/\varepsilon_{ll} = 0.8$, $\varepsilon_{nl}/\varepsilon_{ll} = 0.6$, $\varepsilon_{nn} = 0$, $\alpha = 0.4 M_1^{nc} \sigma^4$, $M_1^c = 0$, $\rho_1(t=0) = 0.9 \pm \xi$ (where ξ represents white noise of amplitude 0.05) and $(\mu - \mu_{coex})/kT = -0.88$, where the liquid exhibits spinodal decomposition–evaporation.

Figure 5 gives snapshots of the evolution of a fingering instability for a retracting dewetting front. At early times the straight front shows a rather short-wave instability; about 16 wiggles can be seen. However, they are only a transient: the finger pattern coarsens rapidly until only about seven fingers remain. The fingering then becomes stationary; i.e., just as in the KMC, the mean finger number remains roughly constant, although new branches are continuously created and old branches join each other. In general, the results on fingering agree well with results obtained using the KMC model [41]. From this we conclude that jamming of discrete particles is not a necessary factor for causing the instability, since the fingering is seen here in a continuum model with a diffusion constant that is independent of the nanoparticle concentration. The DDFT is better suited than the KMC for investigations of the early instability stages: they are easier to discern without the discrete background noise of the KMC. Furthermore, one may perform a linear stability analysis of the one-dimensional undisturbed streamwise front profiles with respect to transverse perturbations (in analogy to the approach used in [86, 87, 19]).

3.3. Thin film hydrodynamics

The previous two sections focused on two approaches to describe the experimentally observed patterning dynamics in the ultrathin postcursor film left behind by a mesoscopic receding dewetting front. Although both the kinetic Monte Carlo model and the dynamical density functional theory are able to describe well the processes in the ultrathin film, they cannot be employed to describe mesoscale hydrodynamics. A relatively simple model for the latter can be derived in the framework of a long-wave or lubrication equation [63, 8]. We will illustrate here the approach by considering an isothermal situation where the nanoparticles are not surface active, i.e. they do not act as surfactants. For a model incorporating the effects of latent heat generation and surface-active particles resulting in thermal and solutal Marangoni stresses, see [88]. A description of spreading particle solutions incorporating a structural disjoining pressure has also been considered [89]. For related work on particle-laden film flow on an incline see [90, 91].

One starts from the Stokes equations, together with continuity, no-slip boundary conditions at the substrate and force equilibria at the free surface, and applies a long-wave approximation. Under the assumption that concentrations equilibrate rapidly over the film thickness, we obtain coupled nonlinear evolution equations for the film thickness profile $h(x, t)$ and the number of nanoparticles per unit length $h_p = \phi h$, where ϕ is the volume concentration of the nanoparticles. Note that h_p corresponds to the local thickness of the nanoparticle layer when all the solvent is evaporated. The resulting evolution equation for the film thickness is equation (1) above, and, focusing on the influence of particle-independent capillarity and wettability only, the energy functional $F[h]$ is given by equation (2) above. Note that the viscosity η depends on the particle concentration.
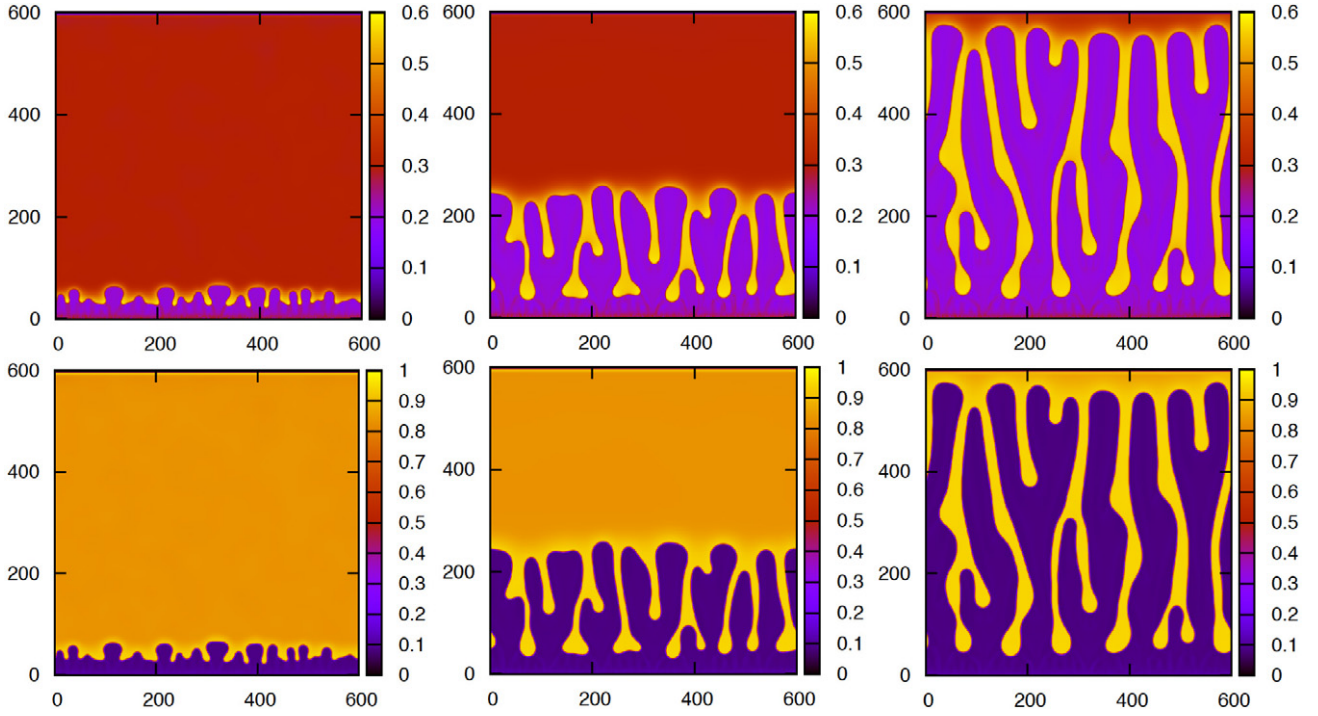
Figure 5. Density profiles for the situation where the substrate is covered by nanoparticles with average density $\rho_n^{av} = 0.3$ and with the liquid excluded from the region $y < 0$. The top row shows the nanoparticle density profiles and the bottom row the corresponding liquid density profiles at the times $t/t_1 = 1000$ (left), $10\,000$ (middle) and $30\,000$ (right), where $t_1 = 1/kT M_1^{nc}\sigma^2$. The parameters are $kT/\varepsilon_{ll} = 0.8$, $\varepsilon_{nl}/\varepsilon_{ll} = 0.6$, $\varepsilon_{nn} = 0$, $\alpha = 0.2M_1^{nc}\sigma^4$, $M_1^c = 0$, $\rho_l(t=0) = 0.9 \pm \xi$ (where ξ represents white noise of amplitude 0.05) and $(\mu - \mu_{coex})/kT = -0.78$.

Following [88, 89, 91, 92] we use the Quemada law for dense suspensions [93–95]

$$\eta(\phi) = \eta_0 \left(1 - \frac{\phi}{\phi_c}\right)^{-2} \qquad (8)$$

where $\phi_c = 0.64$ corresponds to random close packing of spherical particles. For the nanoparticle volume per length $h_p = \phi h$ one obtains the following evolution equation:

$$\partial_t(\phi h) = \nabla\left[\phi Q_c \nabla \frac{\delta F}{\delta h}\right] + \nabla\left[D(\phi)h\nabla\phi\right], \qquad (9)$$

where the particle concentration dependent diffusion coefficient $D(\phi)$ is related to the viscosity by the Einstein relation $D(\phi) = kT/6\pi R\eta(\phi)$, where R is the radius of the nanoparticles [96].

We illustrate results obtained employing this thin film theory using the single example of a receding dewetting front for a partially wetting film. We use the disjoining pressure and material constants for the liquid considered in [57], where the evaporative and convective dewetting of a film of volatile liquid is studied. We add, however, the nanoparticles to the system. The expression that we employ for the local free energy term in equation (2) is

$$f(h) = \frac{S_{LW}d_0^2}{h^2} + S_P \exp\left(\frac{d_0 - h}{l_0}\right), \qquad (10)$$

where the parameters characterizing the interaction between the liquid film and the surface are the apolar and polar

spreading coefficients S_{LW} and S_P, respectively, the Debye length l_0 and the Born repulsion length d_0 [57]. The resulting disjoining pressure $\Pi = -\partial_h f(h)$ allows for a stable precursor film (thickness $h_{precursor}$) and also has a second (larger) thickness (h_0) that corresponds to a secondary minimum of the underlying energy functional. See [11, 97] for studies of film and drop states for similar disjoining pressures. Our results are calculated for a system where the profiles only vary in one Cartesian direction (x), corresponding to a straight dewetting front. However, our results may also be interpreted as applying to a circular flat drop whose front remains circular throughout the dewetting and evaporation process. In this case one should interpret the coordinate x as the distance from the centre of the circular film.

We start with a film of height h_0 of finite length sitting on a precursor film and assume that the film contains nanoparticles at constant concentration ϕ_0. The chosen parameter values ensure that the film of thickness h_0 is linearly stable. As we do not incorporate noise, no nucleation of additional holes can occur (even with noise the probability would be extremely low). Without evaporation the film dewets 'classically' by a retraction of the initially step-like front. After a short time, surface tension smoothes the profile of the receding front and a capillary rim forms that collects all the dewetted liquid. The front recedes until all liquid is collected in a central drop. Since no liquid evaporates ($Q_{nc} = 0$ in equation (1)), the particle concentration does not change during the process.

The situation changes when allowing for evaporation ($Q_{nc} > 0$). Now the front may retract by convection *and/or*
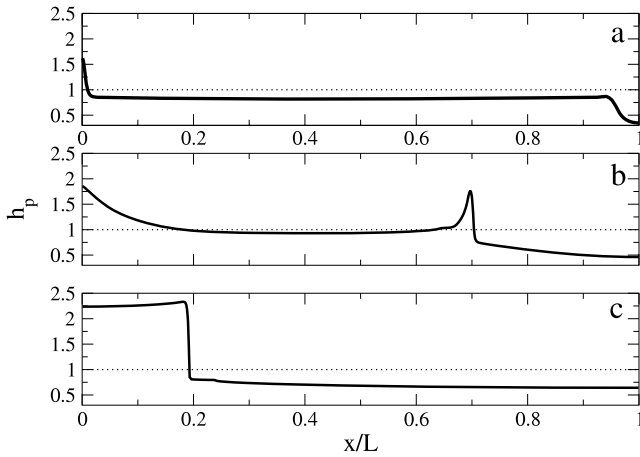
Figure 6. Profiles of the final dried-in nanoparticle layer for the dewetting of a suspension of nanoparticles in a volatile solvent that partially wets the substrate for (a) high ($\Omega = 10^{-3}$), (b) medium ($\Omega = 2 \times 10^{-6}$) and (c) low ($\Omega = 0.78 \times 10^{-8}$) evaporation rates; for the case when $\chi = H/l_0 = 1.09$, the lateral length scale is $\ell = \sqrt{\gamma/\kappa} H$, with $\kappa = (S_P/l_0) \exp(d_0/l_0) H$ being an energy scale related to wettability, and the vertical length scale is $H = \sqrt{2 S_{\mathrm{LW}}/\kappa} d_0$. The remaining dimensionless parameters are the evaporation number $\Omega = Q_e \eta_0 \ell^2 / H^3$, the diffusion number $\Gamma = D(0) \eta_0 / H \kappa = 10^{-4}$ and the dimensionless chemical potential $M = H \mu / \kappa = -0.0035$. The system size is $L = 19\,500\ell$. Film thickness and h_p in the plots are scaled by the precursor film thickness.

Figure 7. A sequence of profiles during a dewetting process with competing evaporation and convection that leads to the dried-in ring structure of nanoparticles displayed in figure 6(b). Profiles are (a) before pinning ($t = 0.08T$), (b) at self-pinning ($t = 0.13T$), and (c) after depinning ($t = 0.29T$), where $T = 3 \times 10^{10}\tau$ with $\tau = \eta_0 \gamma H / \kappa^2$ (T is of the order of 1 s). The film thickness profiles h are the bold solid lines, the nanoparticle concentrations ϕ are the dotted lines and the nanoparticle layer heights $h_p = h\phi$ are the dashed lines. The remaining parameters and scalings are as in figure 6(b).

evaporation. Evaporation leads to the possibility of a strong increase in the particle concentration at the contact line as evaporation is strongest there. Due to the strong nonlinear dependence of the viscosity on the particle concentration, this may lead to a dramatic decrease of the convective contribution to the front velocity. For moderate evaporation rates, this may result in a (temporary) self-pinning of the front. Within the present basic model, the process can (after complete dry-in) result in three different basic deposition patterns. (i) For very fast evaporation rates, all other processes occur over timescales that are much larger. In particular, the effects of convective redistribution of the liquid are negligible. As a result one finds that a nearly homogeneous film of nanoparticles of thickness $h_p = \phi_0 h_0$ is deposited (see figure 6(a)). Convection only results in the small heap of material visible on the left-hand side of figure 6(a). The decrease in h_p on the right side of figure 6(a) arises due to the diffusion of particles to the right of the initial front position. (ii) For very low evaporation rates, the film dynamics is dominated by convective dewetting as this process acts on a much shorter timescale than evaporation. As a result, all the liquid is collected into a drop before evaporation slowly removes the remaining solvent. Under these conditions most of the nanoparticles are deposited in a single heap (see figure 6(c)). Depending on the diffusivity, the heap might be highest at the centre or show a depression there. (iii) At intermediate evaporation rates, one may observe the deposition of a nanoparticle ring around a region with a nanoparticle film of much lower height. At the centre, deposition might increase again (see figure 6(b)).

The most intriguing feature is the ring formation that has been observed experimentally for suspensions of very different
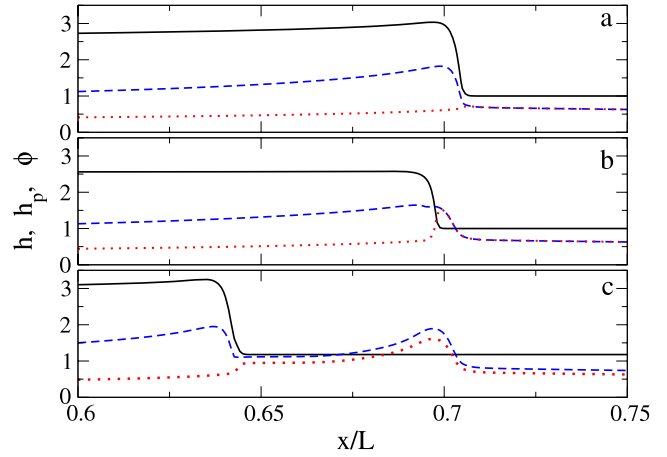
particle sizes ranging from nanometres [32, 46, 47, 36] to hundreds of micrometres. Pinning of the contact line and thermal Marangoni effects are often mentioned as necessary conditions for the ring formation. The contact line pinning is often assumed to result from substrate heterogeneities. Film height and concentration profiles at various instants during the dewetting process are displayed in figure 7. The profiles are from before, at and after self-pinning of the contact line. In figure 8 we display a space–time plot for the complete process. At first, the front recedes in the same manner as when there is no evaporation, but now driven by convection and evaporation. A small capillary rim forms that collects all the dewetted liquid that does not evaporate. The particle concentration slowly increases at the contact line (figure 7(a) and regime (i) in figure 8). The concentration increases further, and when it approaches random close packing ϕ_c the viscosity diverges and the front pins itself. When pinned, further retraction only occurs through evaporation (figure 7(b) and regime (ii) in figure 8). The front eventually depins and starts to move again, leaving a nanoparticle ring behind (figure 7(c) and regime (iii) in figure 8). However, the velocity is not as large as at the beginning, owing to the fact that the mean concentration of particles has increased. The remaining particles are transported to the centre and are deposited there when the remaining solvent evaporates (regime (iv) in figure 8).

The simple model used here shows that (i) the contact line stops due to self-pinning by the deposited particles and (ii) the Marangoni effect is not necessary for the ring formation. The model can easily be refined to account for solutal and/or thermal Marangoni effects [88] but self-pinning should also be investigated further in the simple case presented here.
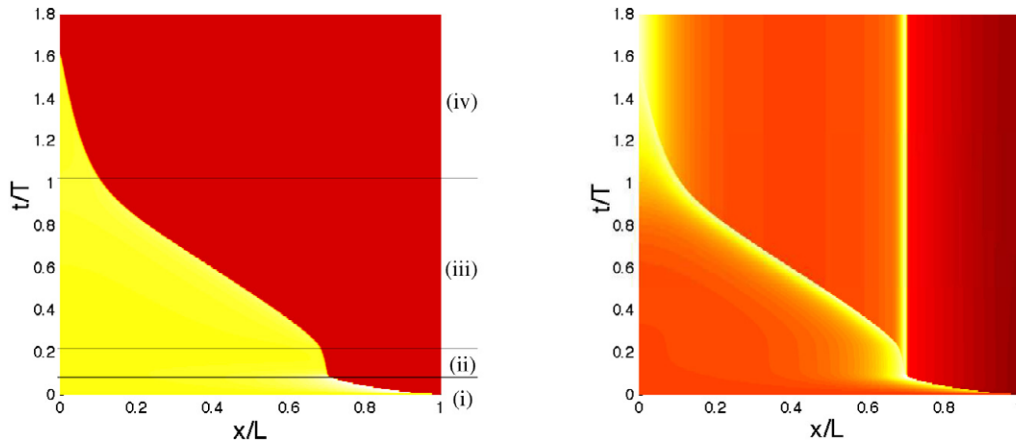
Figure 8. Space–time plots are given for (left) the film thickness h and (right) the nanoparticle layer height $h_p = h\phi$. The plot corresponds to the complete evolution resulting in the ring profile of figure 6(b). In both panels bright (dark) parts denote high (low) regions. The prominent central dark–bright border in the left panel indicates the change of the position of the contact line in time. Over time, four regimes can be distinguished: (i) fast motion before pinning, (ii) nearly no front motion during self-pinning, (iii) slow motion after depinning, and (iv) final evaporation from the centre.

4. Conclusion

We have discussed recent work on pattern formation processes in films and drops of evaporating suspensions/solutions of polymers and particles. After reviewing experiments on suspensions of thiol-coated gold nanoparticles in toluene we have focused on the modelling of the transport and phase change processes involved. A theoretical approach to the modelling of the hydrodynamics on the mesoscale has been described as well as more microscopic models for the dynamics in the observed nanoscopic 'postcursor' film. In particular, we have introduced (i) a microscopic kinetic Monte Carlo model, (ii) a dynamical density functional theory and (iii) a hydrodynamic thin film model.

The kinetic Monte Carlo model and the dynamical density functional theory can both be used to investigate and understand the formation of polygonal networks, spinodal and branched structures resulting from the dewetting of an ultrathin 'postcursor' film that remains behind the mesoscopic dewetting front. They are, however, not capable of describing the dynamical processes in a mesoscopic film. We have seen that the KMC model is able to describe the interplay of solute diffusion within the solvent and solvent evaporation/condensation. It also takes the liquid–liquid, liquid–particle and particle–particle interactions into account and therefore allows us to distinguish different regimes of the transverse (fingering) instability of the evaporative dewetting front: a transport regime where the instability is almost completely independent of the interaction strengths and a demixing regime where particles and liquid demix at the receding front, thereby increasing its transverse instability.

The dynamical density functional theory describes the coupled dynamics of the density fields of the liquid and the nanoparticles. In the form described above (i.e. based on the two-dimensional Hamiltonian (3)) we obtain a simple theory that allows us to study the time evolution of the evaporating ultrathin film and also to investigate the influence

of processes such as surface diffusion by the liquid, which are not incorporated in the KMC model. However, it is straightforward to extend the theory to consider a fully three-dimensional fluid film, in which one can distinguish between short- and long-range interactions of solvent and/or solute with the substrate. We have, however, restricted the examples given here to situations that can also be described using the KMC model. A further exploration will be presented elsewhere.

Finally, we have discussed a simple thin film model for the hydrodynamics on the mesoscale. It results from a long-wave approximation and consists of a pair of coupled evolution equations for the film thickness profile and the mean particle concentration. It has been used to discuss the self-pinning of receding contact lines that is related to the formation of rings of dried-in particles (coffee-stain effect) that frequently occurs when films or drops of solutions or suspensions dewet by the combined effects of convection and evaporation.

One of the primary goals of researchers in this field is the search for simple-to-use techniques that allow one to produce hierarchically structured functional layers for a wide range of applications, such as organic solar cells [98]. This means that the experiments advance very rapidly towards increasingly complex systems. For example, there have been investigations of the influence of the phase behaviour on the drying of droplets of a suspension of hard-sphere colloidal particles and non-adsorbing polymer [99], of the instabilities and the formation of drops in evaporating thin films of binary solutions [100] that may lead to treelike patterns [101], of effects of a secondary phase separation on evaporation-induced pattern formation in polymer films [102], of the influence of an imposed flow on decomposition and deposition processes in a sliding ridge of evaporating solution of a binary polymer mixture [103], and of the influence of rather fast evaporation [104, 105]. These complex experimental systems all represent systems of high practical interest that the theories presented here are not (yet) able to describe. Such experiments do, however, provide a strong motivation for further work to

extend the theories presented here, as well as to develop new approaches.

Let us finally mention several topics that were entirely excluded from our discussion here. First, we focused on a limited range of descriptions and did not, for instance, mention lattice Boltzmann, molecular dynamics or dissipative particle dynamics approaches that may also be employed to describe fluid suspensions [106–109]. Second, we have only discussed spatially homogeneous substrates. Patterned substrates are widely used in dewetting experiments [110–112, 38]. Theoretical descriptions are well developed for the dewetting of films of pure non-volatile liquids on such substrates [113–115, 68, 116–119]. However, in the case of volatile liquids on heterogeneous substrates, much less work has been done. A third topic that we did not touch upon is possible continuum thin film approaches to demixing dewetting suspensions. We believe it is feasible to extend the diffuse interface theories such as model-H [120] to include the influence of evaporation in dewetting nanoparticle suspensions. For instance, such models have already been adapted to describe demixing free surface films of polymer blends [121–123].

Acknowledgments

References

[1] Reiter G 1992 *Phys. Rev. Lett.* **68** 75
[2] Reiter G 1993 *Europhys. Lett.* **23** 579
[3] Sharma A and Reiter G 1996 *J. Colloid Interface Sci.* **178** 383
[4] de Gennes P-G 1985 *Rev. Mod. Phys.* **57** 827
[5] Brochard-Wyart F and Daillant J 1989 *Can. J. Phys.* **68** 1084
[6] Müller-Buschbaum P 2003 *J. Phys.: Condens. Matter* **15** R1549
[7] Seemann R, Herminghaus S, Neto C, Schlagowski S, Podzimek D, Konrad R, Mantz H and Jacobs K 2005 *J. Phys.: Condens. Matter* **17** S267
[8] Thiele U 2007 *Thin films of Soft Matter* ed S Kalliadasis and U Thiele (Wien: Springer) pp 25–93
[9] Xie R, Karim A, Douglas J F, Han C C and Weiss R A 1998 *Phys. Rev. Lett.* **81** 1251
[10] Seemann R, Herminghaus S and Jacobs K 2001 *Phys. Rev. Lett.* **86** 5534
[11] Thiele U, Velarde M G and Neuffer K 2001 *Phys. Rev. Lett.* **87** 016104
[12] Bestehorn M and Neuffer K 2001 *Phys. Rev. Lett.* **87** 046101
[13] Becker J, Grün G, Seemann R, Mantz H, Jacobs K, Mecke K R and Blossey R 2003 *Nat. Mater.* **2** 59
[14] Redon C, Brochard-Wyart F and Rondelez F 1991 *Phys. Rev. Lett.* **66** 715
[15] Seemann R, Herminghaus S and Jacobs K 2001 *Phys. Rev. Lett.* **87** 196101
[16] Fetzer R, Jacobs K, Münch A, Wagner B and Witelski T P 2005 *Phys. Rev. Lett.* **95** 127801
[17] Brochard-Wyart F and Redon C 1992 *Langmuir* **8** 2324
[18] Reiter G and Sharma A 2001 *Phys. Rev. Lett.* **87** 166103
[19] Münch A and Wagner B 2005 *Physica* D **209** 178
[20] Tomlinson C 1870 *Phil. Mag. Ser.* 4 **39** 32
[21] Marangoni C G 1871 *Ann. Phys.* **143** 337
[22] Karthaus O, Grasjö L, Maruyama N and Shimomura M 1999 *Chaos* **9** 308
[23] Gu X, Raghavan D, Douglas J F and Karim A 2002 *J. Polym. Sci.* B **40** 2825
[24] Hong S W, Xia J F and Lin Z Q 2007 *Adv. Mater.* **19** 1413
[25] Liu G, Zhang C F, Zhao J and Zhu Y X 2008 *Langmuir* **24** 7923
[26] Mertig M, Thiele U, Bradt J, Leibiger G, Pompe W and Wendrock H 1997 *Surf. Interface Anal.* **25** 514
[27] Mertig M, Thiele U, Bradt J, Klemm D and Pompe W 1998 *Appl. Phys.* A **66** S565
[28] Thiele U, Mertig M and Pompe W 1998 *Phys. Rev. Lett.* **80** 2869
[29] Maeda H 1999 *Langmuir* **15** 8505
[30] Smalyukh I I, Zribi O V, Butler J C, Lavrentovich O D and Wong G C L 2006 *Phys. Rev. Lett.* **96** 177801
[31] Zhang L, Maheshwari S, Chang H C and Zhu Y X 2008 *Langmuir* **24** 3911
[32] Maillard M, Motte L, Ngo A T and Pileni M P 2000 *J. Phys. Chem.* B **104** 11871
[33] Ge G L and Brus L 2000 *J. Phys. Chem.* B **104** 9573
[34] Moriarty P, Taylor M D R and Brust M 2002 *Phys. Rev. Lett.* **89** 248303
[35] Rabani E, Reichman D R, Geissler P L and Brus L E 2003 *Nature* **426** 271
[36] Govor L V, Reiter G, Parisi J and Bauer G H 2004 *Phys. Rev.* E **69** 061609
[37] Martin C P, Blunt M O and Moriarty P 2004 *Nano Lett.* **4** 2389
[38] Martin C P, Blunt M O, Pauliac-Vaujour E, Stannard A, Moriarty P, Vancea I and Thiele U 2007 *Phys. Rev. Lett.* **99** 116103
[39] Stannard A, Martin C P, Pauliac-Vaujour E, Moriarty P and Thiele U 2008 *J. Chem. Phys.* C **112** 15195
[40] Pauliac-Vaujour E, Stannard A, Martin C P, Blunt M O, Notingher I, Moriarty P J, Vancea I and Thiele U 2008 *Phys. Rev. Lett.* **100** 176102
[41] Vancea I, Thiele U, Pauliac-Vaujour E, Stannard A, Martin C P, Blunt M O and Moriarty P J 2008 *Phys. Rev.* E **78** 041601
[42] Thiele U 1998 Entnetzung von Kollagenfilmen *PhD Thesis* Technische Universität Dresden
[43] Yabu H and Shimomura M 2005 *Adv. Funct. Mater.* **15** 575
[44] Deegan R D, Bakajin O, Dupont T F, Huber G, Nagel S R and Witten T A 1997 *Nature* **389** 827
[45] Adachi E, Dimitrov A S and Nagayama K 1995 *Langmuir* **11** 1057
[46] Deegan R D 2000 *Phys. Rev.* E **61** 475
[47] Deegan R D, Bakajin O, Dupont T F, Huber G, Nagel S R and Witten T A 2000 *Phys. Rev.* E **62** 756
[48] Shmuylovich L, Shen A Q and Stone H A 2002 *Langmuir* **18** 3441
[49] Nguyen V X and Stebe K J 2002 *Phys. Rev. Lett.* **88** 164501
[50] Huang J, Kim F, Tao A R, Connor S and Yang P 2005 *Nat. Mater.* **4** 896
[51] Lee S H, Yoo P J, Kwon S J and Lee H H 2004 *J. Chem. Phys.* **121** 4346
[52] Xu L, Shi T F, Dutta P K and An L 2007 *J. Chem. Phys.* **127** 144704
[53] Xu L, Shi T F and An L J 2008 *J. Chem. Phys.* **129** 044904
[54] Elbaum M and Lipson S G 1994 *Phys. Rev. Lett.* **72** 3562
[55] Samid-Merzel N, Lipson S G and Tannhauser D S 1998 *Phys. Rev.* E **57** 2906
[56] Padmakar A, Kargupta K and Sharma A 1999 *J. Chem. Phys.* **110** 1735
[57] Lyushnin A V, Golovin A A and Pismen L M 2002 *Phys. Rev.* E **65** 021602

[58] Pismen L M 2004 *Phys. Rev.* E **70** 021601
[59] Poulard C, Benichou O and Cazabat A M 2003 *Langmuir* **19** 8828
[60] Gotkis Y, Ivanov I, Murisic N and Kondic L 2006 *Phys. Rev. Lett.* **97** 186101
[61] Pauliac-Vaujour E and Moriarty P 2007 *J. Phys. Chem.* C **111** 16255
[62] Gigault C, Dalnoki-Veress K and Dutcher J R 2001 *J. Colloid Interface Sci.* **243** 143
[63] Oron A, Davis S H and Bankoff S G 1997 *Rev. Mod. Phys.* **69** 931
[64] Thiele U 2009 *J. Phys.: Condens. Matter* at press
[65] Burelbach J P, Bankoff S G and Davis S H 1988 *J. Fluid Mech.* **195** 463
[66] Oron A and Bankoff S G 1999 *J. Colloid Interface Sci.* **218** 152
[67] Schwartz L W, Roy R V, Eley R R and Petrash S 2001 *J. Colloid Interface Sci.* **214** 363
[68] Kargupta K, Konnur R and Sharma A 2001 *Langmuir* **17** 1294
[69] Bestehorn M and Merkt D 2006 *Phys. Rev. Lett.* **97** 127802
[70] Teletzke G F, Davis H T and Scriven L E 1988 *Rev. Phys. Appl.* **23** 989
[71] Israelachvili J N 1992 *Intermolecular and Surface Forces* (London: Academic)
[72] Mitlin V S 1993 *J. Colloid Interface Sci.* **156** 491
[73] Pismen L M and Pomeau Y 2000 *Phys. Rev.* E **62** 2480
[74] Onsager L 1944 *Phys. Rev.* **65** 117
[75] Reiter G 1993 *Langmuir* **9** 1344
[76] Sztrum C G, Hod O and Rabani E 2005 *J. Phys. Chem.* B **109** 6741
[77] Yosef G and Rabani E 2006 *J. Phys. Chem.* B **110** 20965
[78] Gouyet J F, Plapp M, Dieterich W and Maass P 2003 *Adv. Phys.* **52** 523
[79] Marconi U M B and Tarazona P 1999 *J. Chem. Phys.* **110** 8032
[80] Marconi U M B and Tarazona P 2000 *J. Phys.: Condens. Matter* **12** A413
[81] Archer A J and Rauscher M 2004 *J. Phys. A: Math. Gen.* **37** 9325
[82] Archer A J and Evans R 2004 *J. Chem. Phys.* **121** 4246
[83] Monson P A 2008 *J. Chem. Phys.* **128** 084701
[84] Chaikin P M and Lubensky T C 1997 *Principles of Condensed Matter Physics* (Cambridge: Cambridge University Press)
[85] Langer J S 1992 *Solids Far from Equilibrium* ed C Godreche (Cambridge: Cambridge University Press) pp 297–363
[86] Spaid M A and Homsy G M 1996 *Phys. Fluids* **8** 460
[87] Thiele U and Knobloch E 2003 *Phys. Fluids* **15** 892
[88] Warner M R E, Craster R V and Matar O K 2003 *J. Colloid Interface Sci.* **267** 92
[89] Matar O K, Craster R V and Sefiane K 2007 *Phys. Rev.* E **76** 056315
[90] Zhou J J, Dupuy B, Bertozzi A L and Hosoi A E 2005 *Phys. Rev. Lett.* **94** 117803
[91] Cook B P, Bertozzi A L and Hosoi A E 2008 *SIAM J. Appl. Math.* **68** 760
[92] Craster R V, Matar O K and Sefiane K 2009 *Langmuir* **25** 3601–9
[93] Quemada D 1977 *Rheol. Acta* **16** 82
[94] Quemada D and Berli C 2002 *Adv. Colloid Interface Sci.* **98** 51
[95] Stickel J J and Powell R L 2005 *Annu. Rev. Fluid Mech.* **37** 129
[96] Dhont J K G 1996 *An Introduction to Dynamics of Colloids* (Amsterdam: Elsevier)
[97] Thiele U, Velarde M G, Neuffer K and Pomeau Y 2001 *Phys. Rev.* E **64** 031602
[98] Heier J, Groenewold J, Castro F A, Nueesch F and Hany R 2008 *Proc. Soc. Photo-Opt. Instrum. Eng.* **6999** J9991
[99] Haw M D, Gillie M and Poon W C K 2002 *Langmuir* **18** 1626
[100] Govor L V, Parisi J, Bauer G H and Reiter G 2005 *Phys. Rev.* E **71** 051603
[101] Govor L V, Reiter G, Bauer G H and Parisi J 2006 *Phys. Rev.* E **74** 061603
[102] Yamamura M, Nishio T, Kajiwara T and Adachi K 2002 *Chem. Eng. Sci.* **57** 2901
[103] Müller-Buschbaum P, Bauer E, Pfister S, Roth S V, Burghammer M, Riekel C, David C and Thiele U 2006 *Europhys. Lett.* **73** 35
[104] Bormashenko E, Pogreb R, Stanevsky O, Bormashenko Y, Stein T and Gengelman O 2005 *Langmuir* **21** 9604
[105] Bormashenko E, Pogreb R, Stanevsky O, Bormashenko Y, Stein T, Gaisin V Z, Cohen R and Gendelman O V 2005 *Macromol. Mater. Eng.* **290** 114
[106] Gibson J B, Zhang K, Chen K, Chynoweth S and Manke C W 1999 *Mol. Simul.* **23** 1
[107] Stratford K and Pagonabarraga I 2008 *Comput. Math. Appl.* **55** 1585
[108] Drazer G, Khusid B, Koplik J and Acrivos A 2005 *Phys. Fluids* **17** 017102
[109] Kromkamp J, van den Ende D, Kandhai D, van der Sman R and Boom R 2006 *Chem. Eng. Sci.* **61** 858
[110] Rockford L, Liu Y, Mansky P, Russell T P, Yoon M and Mochrie S G J 1999 *Phys. Rev. Lett.* **82** 2602
[111] Sehgal A, Ferreiro V, Douglas J F, Amis E J and Karim A 2002 *Langmuir* **18** 7041
[112] Geoghegan M and Krausch G 2003 *Prog. Polym. Sci.* **28** 261
[113] Lenz P and Lipowsky R 1998 *Phys. Rev. Lett.* **80** 1920
[114] Bauer C, Dietrich S and Parry A O 1999 *Europhys. Lett.* **47** 474
[115] Konnur R, Kargupta K and Sharma A 2000 *Phys. Rev. Lett.* **84** 931
[116] Brinkmann M and Lipowsky R 2002 *J. Appl. Phys.* **92** 4296
[117] Brusch L, Kühne H, Thiele U and Bär M 2002 *Phys. Rev.* E **66** 011602
[118] Thiele U, Brusch L, Bestehorn M and Bär M 2003 *Eur. Phys. J.* E **11** 255
[119] Thiele U 2003 *Eur. Phys. J.* E **12** 409
[120] Anderson D M, McFadden G B and Wheeler A A 1998 *Annu. Rev. Fluid Mech.* **30** 139
[121] Thiele U, Madruga S and Frastia L 2007 *Phys. Fluids* **19** 122106
[122] Frolovskaya O A, Nepomnyashchy A A, Oron A and Golovin A A 2008 *Phys. Fluids* **20** 112105
[123] Madruga S and Thiele U 2009 *Phys. Fluids* at press